Ionics (2021) 27:3837–3846
https://doi.org/10.1007/s11581-021-04110-0

ORIGINAL PAPER

In situ functionally utilize surface residual lithium of Co-free Li-rich layered oxides

Wang Ke[1] · Yunshan Jiang[1] · Yi Han[1] · Liang Deng[1] · Yang Xia[1] · Lanfang Que[1] · Fuda Yu[1] · Yan Wang[1] · Zhenbo Wang[1,2,3]

Received: 24 February 2021 / Revised: 18 April 2021 / Accepted: 19 May 2021 / Published online: 28 June 2021

Abstract

As the candidate cathode material of next-generation lithium-ion batteries (LIBs), Li-rich layered oxides (LLOs) suffer from the problems of surface residual lithium and own insufficient performance as an ionic and electronic conductor. Herein, we propose a strategy for in situ utilization of the residual lithium to form a functionalized sulfur-containing surface coating layer for Co-free LLOs by designated consumption of the residual lithium compounds (Li_2CO_3 and LiOH) with a simple sulfur treatment. The layer significantly improves the lithium-ion diffusion kinetics at high current rates and inhibits the growth of charge transfer resistance. The results of composition and structure characterization prove that the layer mainly containing Li_2SO_4 guides the favorable evolution of particles' bulk crystal structure during the cycle. The modified sample exhibits a higher first coulombic efficiency of 84.4%, excellent rate capabilities, and superior cycle capacity retention of 93.3% after 300 cycles at 250 mA g^{-1}.

Keywords Lithium-ion battery · Co-free lithium-rich layered oxide · Residual lithium · Functional coating layer

Introduction

Lithium-ion batteries (LIBs) are widely used in electric vehicles and hybrid vehicles due to their excellent energy storage characteristics [1–5]. However, facing the industry's pursuit of lower cost and higher energy density in the future, the existing commercial cathodes such as $LiFePO_4$ and $LiCoO_2$ cannot meet the needs [6–8]. Lithium-rich layered oxides (LLO) $xLi_2MnO_3{\cdot}(1\text{-}x)LiMO_2$ (M = Ni, Co and Mn), which exhibit extremely high energy density (> 250 mAh g^{-1}) owing to their higher lithium content and the participation of lattice oxygen in the charge and discharge process, are widely considered as one of the candidate cathode materials for next-generation LIBs. Among them, cobalt-free lithium-rich materials with the advantages like lower cost and others have attracted much attention [9–13]. But because of incomplete utilization during crystallization by roasting, part of excessive lithium will react with CO_2 or H_2O in the air to form Li_2CO_3 or LiOH when it sticks to the surface [14]. On the one hand, it leads to the waste of lithium resources; on the other hand, the CO_2 generated by the decomposition of Li_2CO_3 starting from 3.8 V (vs. Li/Li^+, same below) promotes the formation of a poorly conductive solid electrolyte interphase (SEI) film, which will further weaken the ionic and electronic conductivity of particles and decrease the electrochemical performance of LLO [15–17]. They both hinder the commercial application of lithium-rich materials.

The surface coating strategy can achieve the goal of weakening the influence of Li_2CO_3 and LiOH by building a functional film on the surface of the particle to isolate the

✉ Fuda Yu
yufuda@hit.edu.cn

✉ Yan Wang
wangy_msn@hit.edu.cn

✉ Zhenbo Wang
wangzhb@hit.edu.cn

[1] MIIT Key Laboratory of Critical Materials Technology for New Energy Conversion and Storage, School of Chemistry and Chemical Engineering, State Key Lab of Urban Water Resource and Environment, Harbin Institute of Technology, No.92 West-Da Zhi Street, Harbin 150001, China

[2] College of Materials Science and Engineering, Shenzhen University, Shenzhen 518071, Guangdong, China

[3] Zhuhai Zhongli New Energy Sci-Tech Co., Ltd., Zhuhai 519175, Guangdong, China

surface from the electrolyte [18–22]. However, this method ignores the value of residual lithium by treating it simply as the burden of improving material performance. Considering that LiOH and Li_2CO_3 form a thin coating on the surface of the particles, it is feasible to play a positive effect on the residual lithium by functionalizing the layer [23]. SO_3 can react with LiOH or Li_2CO_3 to form an excellent lithium-ion conductor Li_2SO_4, while reducing the pH value of the particle surface, which is an ideal material for transformation. It has been reported that Li_2O under high temperature conditions is preemptively reacted to form Li_2SO_4 by mixed gas composed of SO_2 and O_2, but there exists a small amount of insufficiently oxidized Li_2SO_3 and $Li_2S_2O_4$ because of the influence coming from reaction environment [14]. In order to avoid the interference of by-products, the calcination process will be carried out under high temperature oxidizing environment. Thus, it is still challenging to develop simple and effective approaches to realize the compositional control of the functionalized surfaces for LLO. More importantly, studies on the effect of in situ formed functionalized surfaces on the composition and structural evolution of LLO during the cycling process are warranted.

Herein, we report a simple strategy to utilize the residual lithium compounds on the surface of Co-free LLO oxides. Through the substitution reaction of SO_3 with Li_2CO_3 and LiOH under high temperature oxidation environment and the deposition of SO_3, a functional layer rich in Li_2SO_4 can be built on the surface of a typical Co-free LLO with the chemical formula $Li_{1.2}Mn_{0.6}Ni_{0.2}O_2$. Based on the composition/structure characterizations and cyclic evolution analysis, it is found that the in situ generated functional surface layer can effectively perform three functions: the first is to reduce the content of Li_2CO_3 and LiOH on the surface of the particles and form a new covering layer; the second is to guide the evolution of particles' crystal structure; the third is to exert its excellent characteristics of conducting lithium ions and inhibit the generation of poor electronic conductors. As expected, the designed LLO cathode with a sulfur-containing surface layer exhibits a larger first coulombic efficiency of 84.4% (in contrast to the original sample of 81.0%), superior cycle capacity retention of 93.3% after 300 cycles at 250 mA g^{-1} (while the original sample is only 78.9%), and excellent rate capabilities. This strategy provides a new solution for the plight of the commercial application of Co-free LLO in LIBs.

Experimental

The Co-free Li-rich layered oxide $Li_{1.2}Mn_{0.6}Ni_{0.2}O_2$ was prepared by co-precipitation. SO_3 gas comes from the thermal decomposition of $K_2S_2O_8$, reaction equation as follows:

$$2K_2S_2O_8(s) \rightarrow 2K_2SO_4(s) + 2SO_3(g) + O_2(g)$$

The reaction process as shown in Fig. 1, 600 ℃, is set in order to obtain a surface with low LiOH or Li_2CO_3 content, while taking out in 100℃ for reducing the total amount of SO_3 deposition. The degree of modification is controlled by the mass ratio of active substance and $K_2S_2O_8$ (keep the active substance at 0.25 g, S-0.5 represents $K_2S_2O_8$ mass at 0.125 g, while S-1.0 and S-2.0 are 0.25 g and 0.50 g, respectively). In addition, for eliminating the interference of influence factors like modification temperature, the comparison sample selects S-0 and named Reference.

The specific details of $Li_{1.2}Mn_{0.6}Ni_{0.2}O_2$ preparation and sample characterization are shown in the Supporting Information.

Results and discussion

Theoretical calculations were used to verify whether the reaction occurs as we expected. According to the standard molar Gibbs free energy of formation ($\Delta_f G^{\Theta}{}_m$) (298 K) data (Supporting Information, Table S1), the $\Delta_f G^{\Theta}$m changes of the main reaction processes that may occur as follows:

$$Li_2CO_3(s) + SO_3(g) \rightarrow Li_2SO_4(s) + CO_2(g) \quad \Delta_f G_m^{\Theta} = 215.9 \mathrm{kJmol}^{-1}$$

$$2LiOH(s) + SO_3(g) \rightarrow Li_2SO_4(s) + H_2O(g) \quad \Delta_f G_m^{\Theta} = 304.5 \mathrm{kJmol}^{-1}$$

$$Li_2SO_3(s) + 1/2O_2(g) \rightarrow Li_2SO_4(s) \quad \Delta_f G_m^{\Theta} = 232.7 \mathrm{kJmol}^{-1}$$

$$Li_2O(s) + SO_3(g) \rightarrow Li_2SO_4(s) \quad \Delta_f G_m^{\Theta} = 391.7 \mathrm{kJ\ mol}^{-1}$$

The results show that not only Li_2CO_3 and LiOH, but also the Li_2SO_3 and Li_2O, produced during the treatment process tends to combine with SO_3 or O_2 gas to form Li_2SO_4. This result is also demonstrated in the powder X-ray diffraction

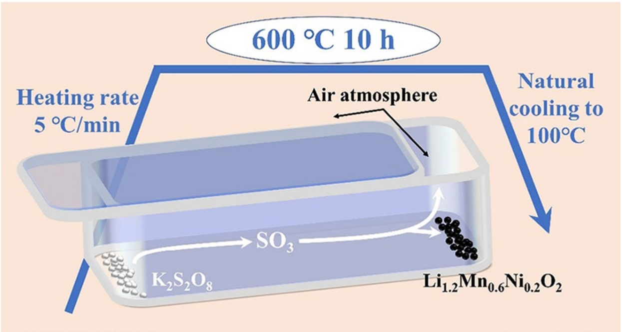

Fig. 1 Schematic diagram of sulfur modification process of the Co-free LLO

(XRD) patterns shown in Fig. 2a and b. No obvious shift is found in each peak after sulfur modification, indicating that the sulfur layer does not significantly affect the particles' crystal structure. What can be also observed is that the diffraction peak intensity of Li_2SO_4 is positively correlated with the total amount of $K_2S_2O_8$ in the part where the degree of incident angle 2θ is 20–30, indicating that our sulfur treatment method and the regulation strategy of Li_2SO_4 production are effective. It is worth noting that if there have no special treatment steps, the strategy of creating a specific gas atmosphere for the gas–solid reaction will inevitably expend the gas-phase reactants that maintain the gas concentration. Especially in an open system, the limited sulfur source will be consumed more to create the reaction environment. The amount of the consumed part and the sulfur source does not always maintain a fixed ratio, which explains why the intensity of the characteristic peak of Li_2SO_4 cannot be maintained at twice the ratio between S-1.0 and S-0.5 as shown in Fig. 2b (the intensity of S-0.5 is less than 1/2 of S-1.0).

A scanning electron microscope (SEM) was used for observing the micron-level morphology of the material before and after sulfur modified, and the results are shown in Fig. 2c, d, e, and f. There is no significant difference in the integral and surface morphology of the particles; the reason is that the SO_3 gas that comes from a very limited $K_2S_2O_8$ decomposition process cannot cause significant changes in particles surface.

Transmission electron microscopy (TEM) was used to confirm the coating state of the particle surface. As shown in Fig. 3a and d, there is a flat thin layer form on the surface of the primary particle after treatment. Observing the edge area of the particles with a high-resolution transmission electron microscope (HRTEM) (Fig. 3b and e), it is obvious that the (003) interplanar spacing of the two particles has increased from the usual 0.47 to about 0.49 nm [24–26], which is related to the high processing temperature. But the difference between the two groups of samples is very small, which means that the SO_3 substitution reaction does not affect the lattice spacing of the particles, which matches the XRD result. After measuring the thickness of the coating layer at different positions, the range is determined to be between 2.0 and 3.0 nm. In the fast Fourier transform (FFT) images of the red frame area containing the thin layer (Fig. 3c and f), it can be observed that (-111) (4.1 Å) and (201) (3.2 Å) crystals related to Li_2SO_4 appear in the S-modified sample [14], what proves the presence of Li_2SO_4 in the coating. Since the production of Li_2SO_4 is limited by the total amount of SO_3, the composition of the thin layer is more complicated and requires further analysis.

In addition, the energy dispersive X-ray spectroscopy image in the scanning transmission electron microscope mode (STEM-EDS) (Fig. 3g) was also used to analyze the processed particles to determine the distribution of S, Mn, Ni, and O elements in the particles. The conclusion that the

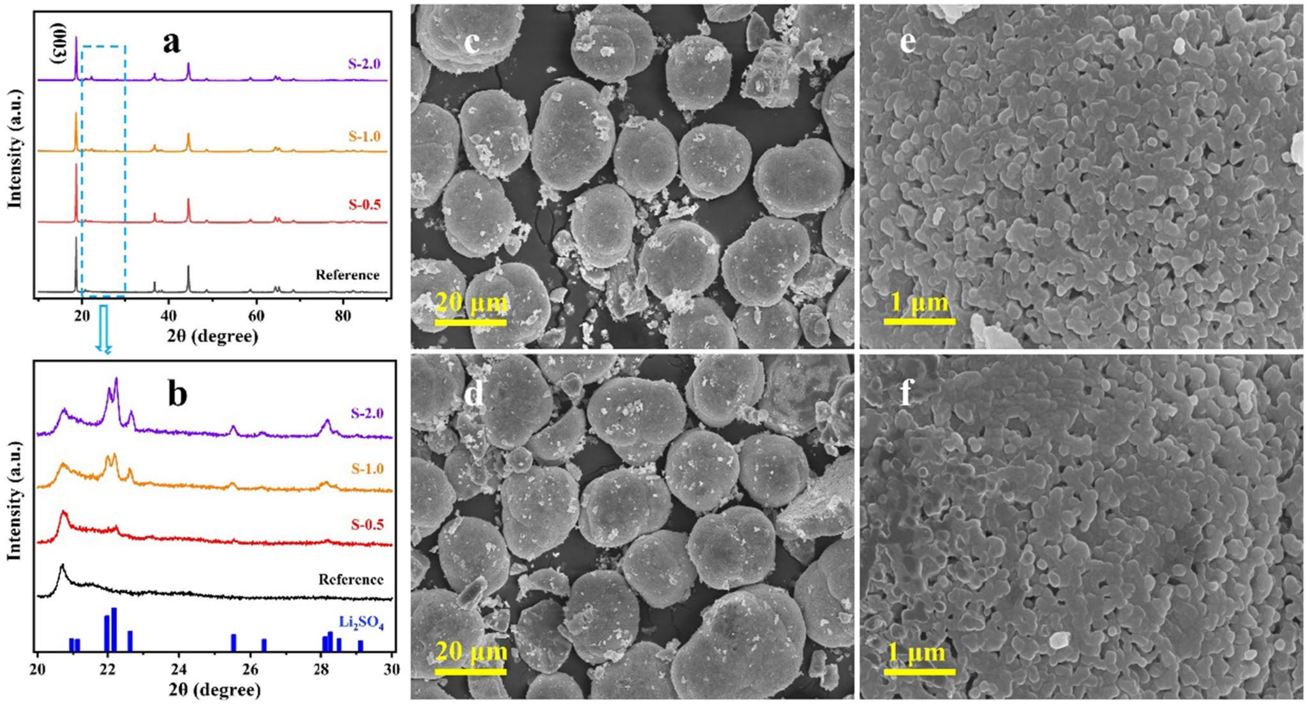

Fig. 2 XRD patterns with the degree of incident angle 2θ are (**a**) 10–90 and (**b**) 20–30, SEM images of samples (**c**, **e**) Reference, and (**d**, **f**) S-modified

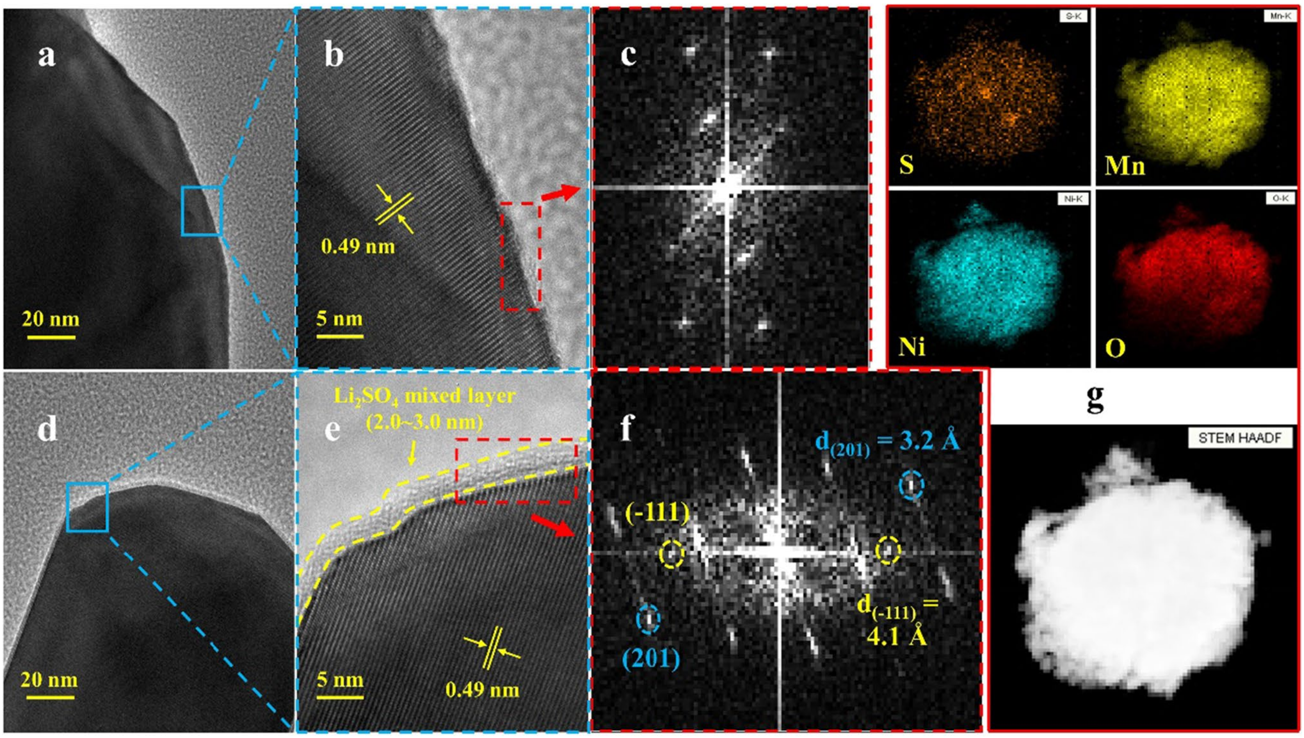

Fig. 3 TEM, HRTEM, and FFT images of (**a**, **b**, and **c**) Reference and (**d**, **e**, and **f**) S-modified, (**g**) STEM-EDS results of S-modified

sulfur-containing mixed layer effectively covers the particle surface can be obtained when the SEM-mapping images (Supporting Information, Fig. S1) were used to analyze together.

X-ray photoelectron spectroscopy (XPS) is used for detailed analysis of the sample surface after SO_3 treatment, and the full spectrums of Reference and S-modified are shown in Fig. 4a. In the core spectra of S 2p (Fig. 4b), the peak position at the binding energy of 169.2 eV indicates that the sulfur on the surface is in the form of SO_4^{2-} instead of S^{2-} or SO_3^{2-} [27]. And it is also confirmed in the O 1 s core spectrum (532.2 eV, including Li_2SO_4 and transition metal sulfate) as shown in Fig. 4c. These results fully demonstrate the effectiveness of this sulfur treatment strategy (the seemingly unchanged intensities of OH^- (531.0 eV, mainly LiOH) and CO_3^{2-} (531.5 eV, mainly Li_2CO_3) can be attributed to the test error of the two samples) [14, 27–29]. In addition, the peak at the binding energy of 533.3 eV in the O 1 s spectrum may correspond to surface adsorption. Besides, it should be noted that there is a small amount of SO_4^{2-} and SO_3^{2-} on the surface before treatment, which is related to the use of sulfate when preparing the precursor. But SO_3^{2-} is almost non-existent after sulfur modification, indicating that the treatment strategy of eliminating by-product in an air environment is effective.

In the core spectra of Mn 2p and Ni 2p (Fig. 4d and e), both the height of Mn^{4+} (643.0 eV) and Ni^{3+} (856.3 eV) peak [30, 31] rise after SO_3 treatment, especially Mn^{4+}, which means that part of the transition metal on the surface reacted. The changes in the relative percentages of Mn^{3+}/Mn^{4+} and Ni^{2+}/Ni^{3+} before and after treatment confirm it. In a word, it can be considered that the main components of the thin layer on the surface of the treated particles are Li_2SO_4, Li_2CO_3, LiOH, and transition metal sulfate.

Generally, the surface treatment will affect the change process of samples' crystal structure during the cycle. Therefore, exploring their changing tendency and the state of surface layer (not only sulfur modified membrane, but also cathode electrolyte interphase (CEI) film) under different cycle periods will help to understand the function of the coating layer after treatment and materials' electrochemical behavior in more detail. The finished half-cells need to go through three processes successively: be placed for 6 h, then activate 3 cycles with a current density of 0.1 C (1 C = 250 mA g^{-1}), and cycle at 1 C at last. The XRD test results of the two groups of cathode pieces under different conditions are shown in Fig. 5a and e. It is observed that the intensity of the lithium-rich characteristic peak of S-modified is always weaker than Reference in every state, which means that the phase evolution in S-modified particles performs more significantly. Moreover, the weakening of the peak intensity corresponding to the (003) crystal plane mainly occurs in activation process and first cycle at 1 C, which indicates that the layered structure has undergone

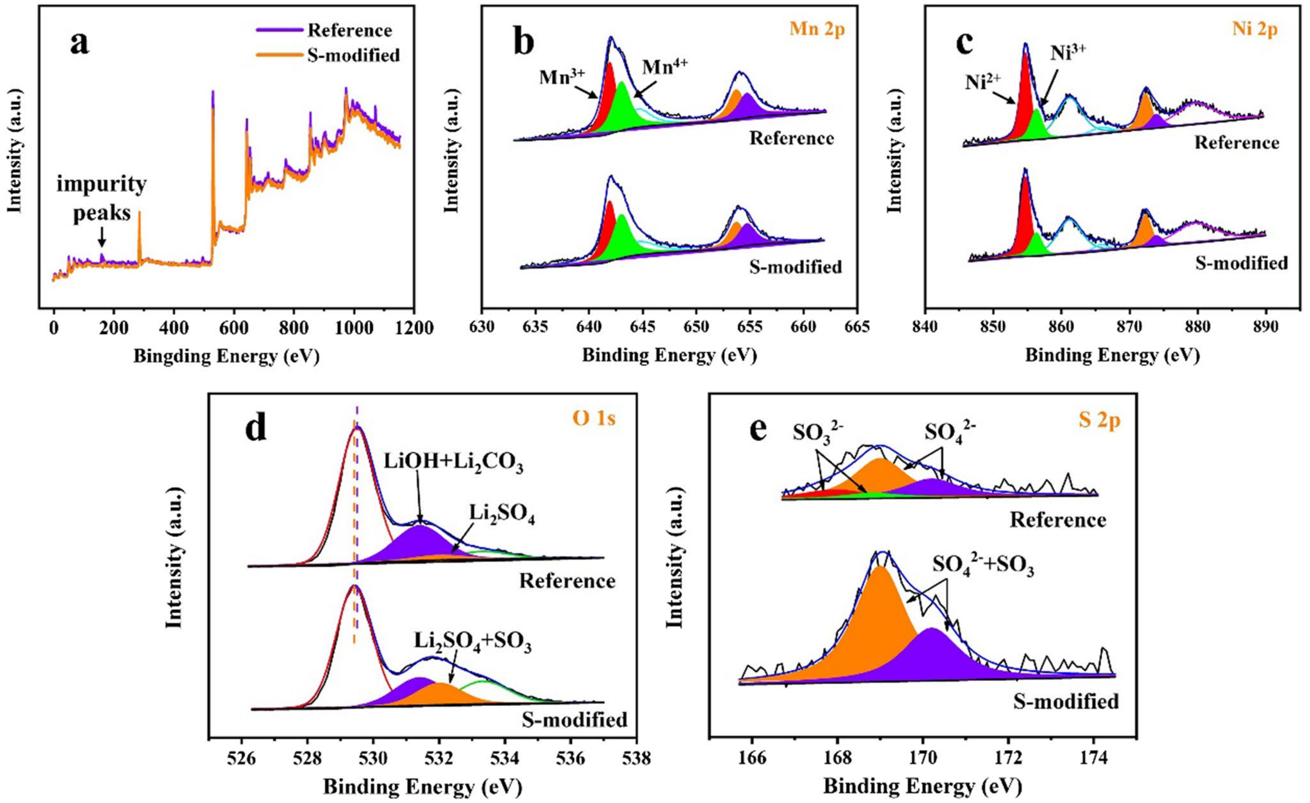

Fig. 4 XPS spectrums of (**a**) full scan, (**b**) S 2p, (**c**) O 1 s, (**d**) Mn 2p, and (**e**) Ni 2p. (**f**) The relative percentages of different valence states of transition metals before and after treatment

major changes at this stage. In the enlarged XRD images with an incident angle 2θ of 20 ~ 30°, the characteristic peak of Li_2SO_4 in Reference that gradually increases can be attributed to the residual SO_4^{2-} and combines with Li^+ during the cycle (Fig. 5b). Nonetheless, the Li_2SO_4 peak of S-modified sample increases significantly during the activation and first cycle at 1C, and then remained basically unchanged (excluding the Li_2SO_4 existing in the particles) (Fig. 5f). The fact indicates that there is a significantly new combination process of Li_2SO_4 formed by SO_4^{2-} and Li^+ at this stage. The new reaction process may be related to the presence of sulfate ions that are not bound to lithium on the surface. In addition, a detailed analysis of the XRD test results shows that the two groups of samples exhibit different phase evolution trends during the cycle (Fig. 5c, d, g, and h). For example, it can be seen that the peaks correspond to the crystal planes of (101) and (103) and weaken faster after sulfur treatment. And there is also the appearance and disappearance of peaks near the two characteristic peaks. The more violent phase evolution degree of the S-modified sample may suggest that its crystal structure has changed greatly compared with the initial state.

The changes in the surface state and crystal structure of Reference and S-modified after 300 cycles at 1 C can be clearly observed in TEM images. In Fig. 5i, the CEI film can be clearly seen on the particle surface of Reference, while the surface coating layer of the sulfur-treated sample (Fig. 5k) has a significant thickness increase (from 2.0 ~ 3.0 to 20.0 ~ 30.0 nm). On the one hand, this phenomenon can be partly attributed to the combination of SO_4^{2-} and Li^+ during cycles; on the other hand, it is related to the formation of CEI film on the surface of the Li_2SO_4 coating layer. The images of HRTEM and the local FFT are shown in Fig. 5j and l. After cycles, Reference still maintains a layered structure with clearly visible lattice fringes of (003) crystal planes, while the main crystal plane of sulfur-treated sample cannot be easily observed after significant phase evolution. These results correspond to changes in peak intensity in XRD.

Figure 6a shows the complete charge and discharge curves about first cycle of Reference, S-0.5, S-1.0, and S-2.0 at 0.1 C. Partially, pre-oxidized of transition metal especially Ni^{2+} during the sulfur modification process can be observed in the XPS spectrum, and it is shown in the charging curves in the form of reduction in the capacity contributed by them (enlarged image in blue frame as shown in Supporting Information Fig. S2) [32–34]. Sulfur can combine with lattice oxygen during the delithiation process to

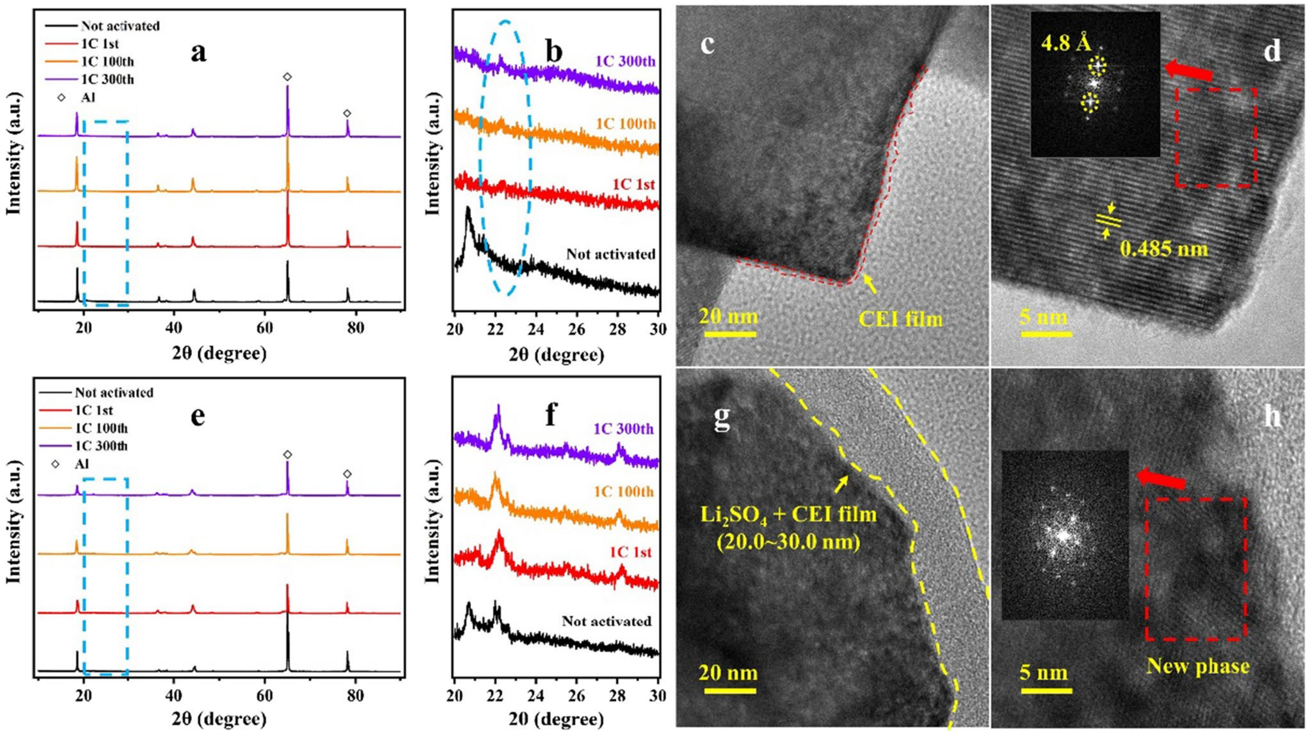

Fig. 5 XRD patterns in different states of (**a**, **b**, **c**, and **d**) Reference and (**e**, **f**, **g**, and **h**) S-modified, TEM, and HRTEM images after 300 cycles of (**i**, **j**) Reference and (**k**, **l**) S-modified

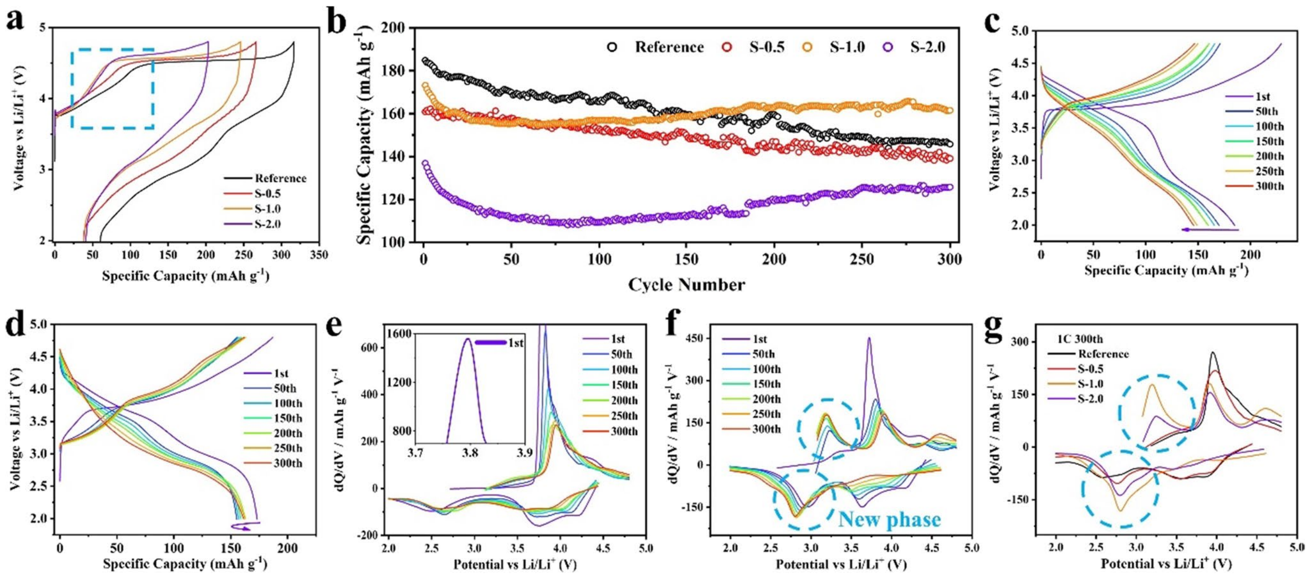

Fig. 6 **a** Initial charge–discharge curves, **b** cycle performance for 300 cycles at 1 C, charge–discharge profiles, and corresponding dQ/dV curves of (**c**, **e**) Reference and (**d**, **f**) S-1.0, and (**g**) dQ/dV profiles at the 300th cycle at 1 C

inhibit the irreversible oxygen release as reported, which is manifested as a shortened platform length near 4.5 V in the first charging curves (Supporting Information Fig. S3) [27]. All in all, moderate sulfur modification helps to improve the first coulombic efficiency (FCE) of the particles (Reference is 81.0%, while S-0.5 and S-1.0 are 85.7% and 84.4%, respectively). Moreover, it also helps to improve the electrochemical stability of the material (Fig. 6b and Fig. S4 in

Supporting Information). After the phase evolution process is relatively stable, the capacity released by S-1.0 changes from rapid decay to gradual increase (the reason why S-0.5 sample shows different tendency can be attributed to a low degree of vulcanization). Among them, the capacity retention rate of S-1.0 after 300 cycles is 93.3% (Reference is 78.9%).

Figure 6c and d show the charge and discharge curves of Reference and S-1.0 at different cycles, and the corresponding differential capacitance (dQ/dV) curves are shown in Fig. 6e and f. The new charging peak of the S-1.0 sample near 3.15 V also contributes the capacity of a similar value during the discharge process, which shows good reversibility. This explains why the generation of new phase will increase the capacity during charging and discharging. Meanwhile, only S-1.0 and S-2.0 samples with a unique capacity change law have new peaks near 3.15 V (charge) and 2.8 V (discharge), which further proves our inference on the reason for the capacity increase of materials (Fig. 6g).

In addition, it is obvious that new reaction has the fastest growth in the process of rapid phase evolution. Combining XRD and TEM images (Fig. 5c, d, g, h, j, and l), we can associate the rapid decay of the discharge-specific capacity of S-1.0 and S-2.0 in the initial stage with the violent evolution of the crystal structure in the process. Both of them are related to the activation process of the material under high current (1 C), as observed in other experiments [35–38]. That is, the processed sample cannot release the capacity that can be released in a stable state in the first cycle after the current density increases. The materials need to experience several cycles to reach a stable state at the new current density which is named activation process. Comparing with other treatment methods, the stable state of the sample after SO_3 treatment shows a unique varying law of gradual increase in capacity. When the activation process is complete, new redox reactions slowly increase, and the phase evolution of the sample is no longer intense. Considering that the S-0.5 sample with low vulcanization degree did not show a similar change process, it can be deliberated that moderate sulfur treatment will change the initial stable state of the sample under high current and endows the sample with a more robust crystal structure in the subsequent cycle process.

The rate performances of four samples at rates of 0.1, 0.2, 0.5, 1, 2, and 5 C are shown in Fig. 7a. At low rates, the capacity decreases with the sulfur increases, which can attribute to a higher resistance caused by coating layer to delithiation process at low rates than positive effects to Li^+ diffusion. At high rates like 1, 2, and 5 C, the gaps between S-modified and Reference are reduced, while the S-1.0 sample is significantly higher than Reference, suggesting that the contrast has reversed [39]. This partly explains why there is almost no difference in cycle performance between Reference and S-1.0 at 2 C (Supporting Information, Fig. S5). To

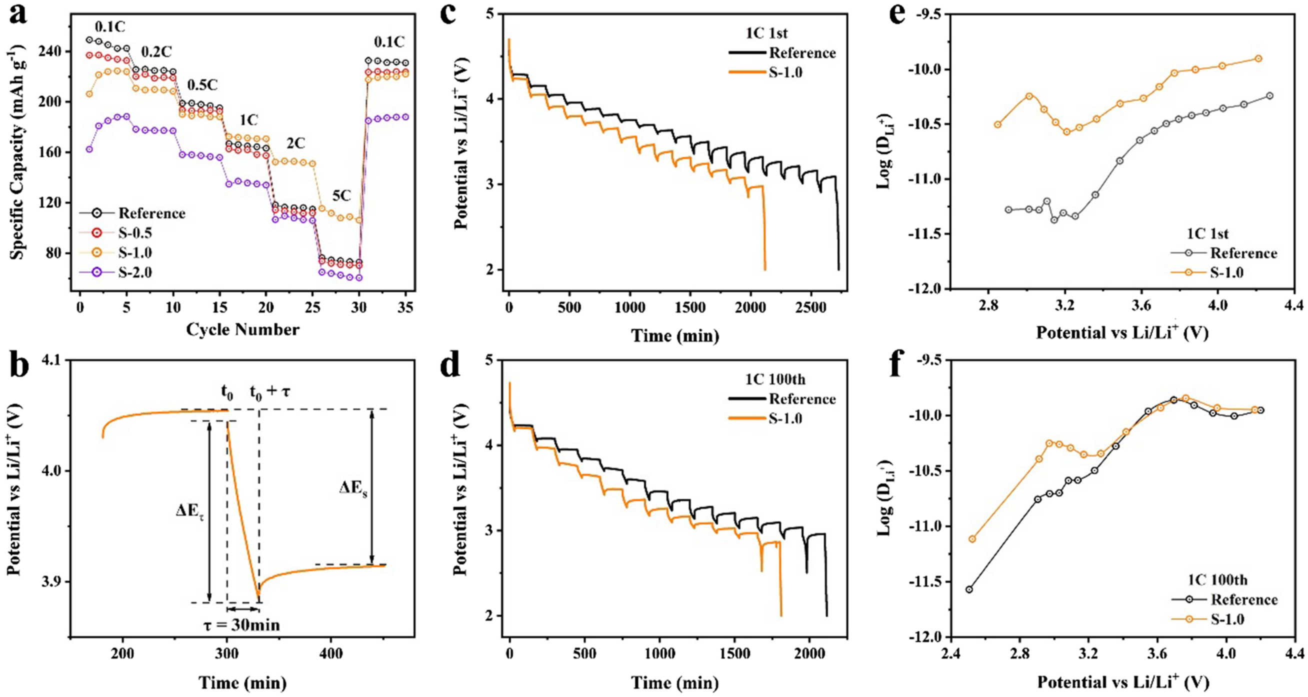

Fig. 7 **a** Rate performances of four samples, **b** a representative single titration at 4.04 V during GITT measurement, GITT discharge test profiles, and corresponding D_{Li^+} of (**c**, **e**) Reference and (**d**, **f**) S-1.0 after 1st cycle and 100th cycle

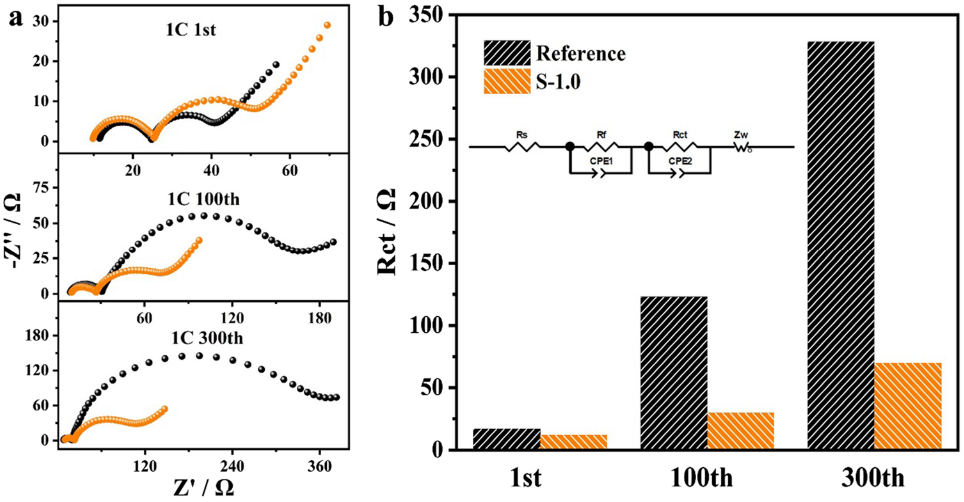

Fig. 8 a EIS profiles of Reference and S-1.0 after different cycles. b R_{ct} values of Reference and S-1.0 after different cycles and the equivalent circuits

verify the point about Li^+ kinetics, we investigated the Li^+ diffusion coefficient (D_{Li^+}) values of Reference and S-1.0 by using galvanostatic intermittent titration technique (GITT) and the following calculation formula:

$$D_{Li^+} = \frac{4}{\pi\tau}\left(\frac{m_B V_M}{M_B S}\right)^2\left(\frac{\Delta E_s}{\Delta E_\tau}\right)^2$$

among them, m_B, M_B, V_M, and S stand for the molecular weight, molecular mass, molar volume of LLO, and active surface area, respectively. Figure 7b shows the ΔE_s and ΔE_τ of the GITT discharge process, while the GITT discharge test profiles of Reference and S-1.0 after 1st cycle and 100th cycle at 1 C as shown in Fig. 7c and d, respectively. The ΔE_s and ΔE_τ values of GITT curves are shown in Table S2a and b (Supporting Information, Table S2), and the D_{Li^+} calculation results obtained based on them are shown in Fig. 7e and f. After 1st cycle at 1 C, the difference of crystal structure between two samples is not significant, which means that the significantly higher D_{Li^+} values of S-1.0 can be attributed to the surface functional layer. Although the difference of D_{Li^+} between two samples shrinks after 100th cycle, S-1.0, which has undergone a crystal structure evolution, still has some advantages over Reference which maintains a layered structure. Both facts highlight the significant promotion effect of the functional layer on the diffusion of lithium ions.

In the LLO system, irreversible extraction of oxygen from particle lattice will induce the carbonate-based electrolyte to generate CO_2 and other substances, resulting in the formation of a poorly conductive SEI film in the electrolyte/electrode interface and increasing the values of charge transfer resistance (R_{ct}) [16]. In fact, Li_2CO_3, the reaction product of the remaining lithium on the surface, can also decompose itself during the cycle and cause similar results [17]. Surface sulfur treatment has been proven to effectively reduce the production of O_2 and CO_2 [14]. Therefore, it can be expected that the sulfur-modification samples will have lower R_{ct} values during cycling. To verify it, electrochemical impedance spectra (EIS) were used to provide a view about the resistance of Reference and S-1.0 under different cycles at 1 C and the results are shown in Fig. 8a (all half-cells are charged to a voltage of 4 V before testing). The curve is consisted of two consequent semicircles and one pitched line while they all represent different meanings: R_Ω is expressed as the intercept of the first semicircle while the semicircle itself represents the resistance R_f (Li^+ migration in SEI and surface-modified layer) in the high frequency region; the second semicircle represents the resistance R_{ct} in the middle frequency region; the bottom line in the low-frequency means Warburg impedance Z_w which relates to the diffusion of Li^+ in the particle bulk [18, 40, 41]. The R_{ct} values and the equivalent circuits obtained by fitting the impedance diagram are shown in Fig. 8b. What can be clearly observed is that the S-1.0 has a slower R_{ct} values and growth rate, which is in line with expectations.

Conclusion

In summary, a strategy for in situ utilization of surface residual lithium to form a functionalized sulfur-containing surface coating layer has been proposed for Co-free LLO. This in situ generated functional surface layer has been constructed by designated consumption of the Li_2CO_3 and LiOH through a simple sulfur treatment. Benefit from the lower charge transfer resistance, higher Li^+ diffusion coefficient, and more stable evolutionary crystal structure, the LLO sample with the in situ functionalized sulfur-containing surface layer exhibits a higher first coulombic efficiency of 84.4% (in contrast to the original sample of 81.0%), excellent rate capabilities, and superior cycle capacity retention of 93.3% after 300 cycles at 250 mA g^{-1} (while the original sample is only 78.9%). These results reveal that the design of an in situ generated functional surface layer can effectively enhance the electrochemical performance and might provide a new solution for the plight of the commercial application of Co-free LLO in LIBs.

Supplementary Information The online version contains supplementary material available at https://doi.org/10.1007/s11581-021-04110-0.

Funding We acknowledge the National Natural Science Foundation of China (Grant No. 51902072, 21673064, and 22075062), China Postdoctoral Science Foundation (Grant No. 2017M621285 and 2018T110292), Fundamental Research Funds for the Central Universities (Grant No. HIT. NSRIF. 2019040 and 2019041), State Key Laboratory of Urban Water Resource and Environment (Harbin Institute of Technology No. 2020DX11), and Zhuhai Innovative and Entrepreneurial Research Team Program (No. ZH01110405180053PWC).

References

1. Zuo WH, Luo MZ, Liu XS, Wu J, Liu HD, Li J, Winter M, Fu RQ, Yang WL, Yang Y (2020) Li-rich cathodes for rechargeable Li-based batteries: reaction mechanisms and advanced characterization techniques. Energy Environ Sci 13:4450–4497
2. Bi YJ, Tao JH, Wu YQ, Li LZ, Xu YB, Hu EY, Wu BB, Hu JT, Wang CM, Zhan JG, Qi Y, Xiao J (2020) Reversible planar gliding and microcracking in a single-crystalline Ni-rich cathode. Science 370:1313–1317
3. Saha S, Assat G, Sougrati MT, Foix D, Li HF, Vergnet J, Turi S, Ha Y, Yang WL, Cabana J, Rousse G, Abakumov AM, Tarascon JM (2019) Exploring the bottlenecks of anionic redox in Li-rich layered sulfides. Nat Energy 4:977–987
4. Zhang K, Han XP, Hu Z, Zhang XL, Tao ZL, Chen J (2015) Nanostructured Mn-based oxides for electrochemical energy storage and conversion. Chem Soc Rev 44:699–728
5. Zheng JM, Myeong SJ, Cho WR, Yan PF, Xiao J, Wang CM, Cho J, Zhang JG (2017) Li- and Mn-rich cathode materials: challenges to commercialization. Adv Energy Mater 7:1601284
6. Wang XX, Ding YL, Deng YP, Chen ZW (2020) Ni-rich/Co-poor layered cathode for automotive Li-ion batteries: promises and challenges. Adv Energy Mater 10:1903864
7. Zhang JC, Cheng FY, Chou SL, Wang JL, Gu L, Wang H, Yoshikawa H, Lu Y, Chen J (2019) Tuning oxygen redox chemistry in Li-rich Mn-based layered oxide cathodes by modulating cation arrangement. Adv Mater 31:1901808
8. Yu HJ, So YG, Kuwabara A, Tochigi E, Shibata N, Kudo T, Zhou HS, Ikuhara Y (2016) Crystalline grain interior configuration affects lithium migration kinetics in Li-rich layered oxide. Nano Lett 16:2907–2915
9. Sun G, Yu FD, Zhao CT, Yu RZ, Farnum S, Shao GJ, Sun XL, Wang ZB (2021) Decoupling the voltage hysteresis of Li-rich cathodes: electrochemical monitoring, modulation anionic redox chemistry and theoretical verifying. Adv Funct Mater 31:2002643
10. Jiang WJ, Zhang CX, Feng YZ, Wei B, Chen LB, Zhang RF, Ivey DG, Wang P, Wei WF (2020) Achieving high structure and voltage stability in cobalt-free Li-rich layered oxide cathodes via selective dual-cation doping. Energy Storage Mater 32:37–45
11. Hy S, Liu HD, Zhang MH, Qian DN, Hwang BJ, Meng YS (2016) Performance and design considerations for lithium excess layered oxide positive electrode materials for lithium ion batteries. Energy Environ Sci 9:1931–1954
12. Nayak PK, Erickson EM, Schipper F, Penki TR, Munichandraiah N, Adelhelm P, Sclar H, Amalraj F, Markovsky B, Aurbach D (2018) Review on challenges and recent advances in the electrochemical performance of high capacity Li- and Mn-rich cathode materials for Li-ion batteries. Adv Energy Mater 8:1702397
13. Sharifi-Asl S, Yurkiv V, Gutierrez A, Cheng M, Balasubramanian M, Mashayek F, Croy J, Shahbazian-Yassar R (2020) Revealing grain-boundary-induced degradation mechanisms in Li-rich cathode materials. Nano Lett 20:1208–1217
14. Seong WM, Cho KH, Park JW, Park H, Eum D, Lee MH, Kim ISS, Lim J, Kang K (2020) Controlling residual lithium in high-nickel (>90%) lithium layered oxides for cathodes in lithium-ion batteries. Angew Chem Int Edit 59:18662–18669
15. Renfrew SE, McCloskey BD (2017) Residual lithium carbonate predominantly accounts for first cycle CO_2 and CO outgassing of Li-stoichiometric and Li-rich layered transition-metal oxides. J Am Chem Soc 139:17853–17860
16. Zhang XD, Shi JL, Liang JY, Yin YX, Zhang JN, Yu XQ, Guo YG (2018) Suppressing surface lattice oxygen release of Li-rich cathode materials via heterostructured spinel $Li_4Mn_5O_{12}$ coating. Adv Mater 30:1801751
17. Mahne N, Renfrew SE, McCloskey BD, Freunberger SA (2018) Electrochemical oxidation of lithium carbonate generates singlet oxygen. Angew Chem Int Edit 57:5529–5533
18. Xiao BW, Wang BQ, Liu J, Kaliyappan K, Sun Q, Liu YL, Dadheech G, Balogh MP, Yang L, Sham TK, Li RY, Cai M, Sun XL (2017) Highly stable $Li_{1.2}Mn_{0.54}Co_{0.13}Ni_{0.13}O_2$ enabled by novel atomic layer deposited $AlPO_4$ coating. Nano Energy 34:120–130
19. Lee M-J, Lho E, Oh P, Son Y, Cho J (2017) Simultaneous surface modification method for $0.4Li_2MnO_3$-$0.6LiNi_{1/3}Co_{1/3}Mn_{1/3}O_2$ cathode material for lithium ion batteries: acid treatment and $LiCoPO_4$ coating. Nano Res 10:4210–4220
20. Chen Z, Kim G-T, Bresser D, Diemant T, Asenbauer J, Jeong S, Copley M, Behm RJ, Lin J, Shen Z, Passerini S (2018) $MnPO_4$-coated $Li(Ni_{0.4}Co_{0.2}Mn_{0.4})O_2$ for lithium(-ion) batteries with outstanding cycling stability and enhanced lithiation kinetics. Adv Energy Mater 8:1801573
21. Zhou L, Yin Z, Tian H, Ding Z, Li X, Wang Z, Guo H (2018) Spinel-embedded and Li_3PO_4 modified $Li[Li_{0.2}Mn_{0.54}Ni_{0.13}Co_{0.13}]O_2$ cathode materials for high-performance Li-ion battries. Appl Surf Sci 456:763–770
22. Yang S-q, Wang P-b, Wei H-x, Tang L-b, Zhang X-h, He Z-j, Li Y-j, Tong H, Zheng J-c (2019) $Li_4V_2Mn(PO_4)_4$-stablized $Li[Li_{0.2}Mn_{0.54}Ni_{0.13}Co_{0.13}]O_2$ cathode materials for lithium ion batteries. Nano Energy 63:103889
23. Liu W, Li XF, Hao YC, Xiong DB, Shan H, Wang JJ, Xiao W, Yang HJ, Yang H, Kou L, Tian ZY, Shao L, Zhang C (2021) Functional passivation interface of $LiNi_{0.8}Co_{0.1}Mn_{0.1}O_2$ toward superior lithium storage. Adv Funct Mater 2008301
24. Yu F-D, Que L-F, Wang Z-B, Xue Y, Zhang Y, Liu B-S, Gu D-M (2017) Controllable synthesis of hierarchical ball-in-ball hollow microspheres for a high performance layered Li-rich oxide cathode material. J Mater Chem A 5:9365–9376
25. Wang M-J, Yu F-D, Sun G, Wang J, Zhou J-G, Gu D-M, Wang Z-B (2019) Co-regulating the surface and bulk structure of Li-rich layered oxides by a phosphor doping strategy for high-energy Li-ion batteries. J Mater Chem A 7:8302–8314
26. Zheng H, Hu Z, Liu P, Xu W, Xie Q, He W, Luo Q, Wang L, Gu D, Qu B, Zhu Z-Z, Peng D-L (2020) Surface Ni-rich engineering towards highly stable $Li_{1.2}Mn_{0.54}Ni_{0.13}Co_{0.13}O_2$ cathode materials. Energy Storage Mater 25:76–85
27. Chen Q, Pei Y, Chen H, Song Y, Zhen L, Xu CY, Xiao P, Henkelman G (2020) Highly reversible oxygen redox in layered compounds enabled by surface polyanions. Nat Commun 11:3411
28. Erickson EM, Sclar H, Schipper F, Liu J, Tian R, Ghanty C, Burstein L, Leifer N, Grinblat J, Talianker M, Shin J-Y, Lampert

JK, Markovsky B, Frenkel AI, Aurbach D (2017) High-temperature treatment of Li-Rich cathode materials with ammonia: improved capacity and mean voltage stability during cycling. Adv Energy Mater 7:1700708

29. McCalla E, Abakumov AM, Saubanere M, Foix D, Berg EJ, Rousse G, Doublet ML, Gonbeau D, Novak P, Van Tendeloo G, Dominko R, Tarascon JM (2015) Visualization of O-O peroxo-like dimers in high-capacity layered oxides for Li-ion batteries. Science 350:1516–1521
30. Song B, Liu Z, Lai MO, Lu L (2012) Structural evolution and the capacity fade mechanism upon long-term cycling in Li-rich cathode material. Phys Chem Chem Phys 14:12875–12883
31. Li J, Xiong S, Liu Y, Ju Z, Qian Y (2013) Uniform LiNi1/3Co1/3Mn1/3O2 hollow microspheres: designed synthesis, topotactical structural transformation and their enhanced electrochemical performance. Nano Energy 2:1249–1260
32. Zhu Z, Yu D, Yang Y, Su C, Huang Y, Dong Y, Waluyo I, Wang B, Hunt A, Yao X, Lee J, Xue W, Li J (2019) Gradient Li-rich oxide cathode particles immunized against oxygen release by a molten salt treatment. Nat Energy 4:1049–1058
33. Zhu Z, Gao R, Waluyo I, Dong Y, Hunt A, Lee J, Li J (2020) Stabilized Co-free Li-rich oxide cathode particles with an artificial surface prereconstruction. Adv Energy Mater 10:2001120
34. House RA, Rees GJ, Pérez-Osorio MA, Marie J-J, Boivin E, Robertson AW, Nag A, Garcia-Fernandez M, Zhou K-J, Bruce PG (2020) First-cycle voltage hysteresis in Li-rich 3d cathodes associated with molecular O_2 trapped in the bulk. Nat Energy 5:777–785
35. Wang MJ, Yu FD, Sun G, Gu DM, Wang ZB (2019) A collaboration of surface protection and bulk doping for high-performance Li-rich cathode materials. ChemistrySelect 4:6256–6264
36. Cheng FQ, Chen JT, Zhou HH, Manthiram A (2013) Structural and electrochemical characterization of $(NH_4)_2HPO_4$-treated lithium-rich layered $Li_{1.2}Ni_{0.2}Mn_{0.6}O_2$ cathodes for lithium-ion batteries. J Electrochem Soc 160:A1661–A1667
37. Zheng J, Deng SN, Shi ZC, Xu HJ, Xu H, Deng YF, Zhang Z, Chen GH (2013) The effects of persulfate treatment on the electrochemical properties of $Li[Li_{0.2}Mn_{0.54}Ni_{0.13}Co_{0.13}]O_2$ cathode material. J Power Sources 221:108–113
38. Rowe AW, Dahn JR (2014) Positive electrode materials in the Li-Mn-Ni-O system exhibiting anomalous capacity growth during extended cycling. J Electrochem Soc 161:A308–A317
39. Wu T, Liu X, Zhang X, Lu Y, Wang B, Deng Q, Yang Y, Wang E, Lyu Z, Li Y, Wang Y, Lyu Y, He C, Ren Y, Xu G, Sun X, Amine K, Yu H (2021) Full concentration gradient-tailored Li-rich layered oxides for high-energy lithium-ion batteries. Adv Mater 33:2001358
40. Wu Z, Ji S, Liu T, Duan Y, Xiao S, Lin Y, Xu K, Pan F (2016) Aligned Li^+ tunnels in core-shell $Li(Ni_xMn_yCo_z)O_2$@$LiFePO_4$ enhances its high voltage cycling stability as Li-ion battery cathode. Nano Lett 16:6357–6363
41. Jiang Y-S, Sun G, Yu F-D, Que L-F, Deng L, Meng X-H, Wang Z-B (2019) Surface modification by fluorine doping to increase discharge capacity of $Li_{1.2}Ni_{0.2}Mn_{0.6}O_2$ cathode materials. Ionics 26:151–161